Influence of non-metallic inclusions on the high cycle fatigue strength of steels

INFLUENCE OF NON-METALLIC INCLUSIONS ON THE HIGH CYCLE FATIGUE STRENGTH OF STEELS

Sabrina Vantadori[a*], Camilla Ronchei[b], Daniela Scorza[c], Andrea Zanichelli[a], Lucas Carneiro Araújo[d], José Alexander Araújo[d]

[a] Department of Engineering & Architecture, University of Parma, Parco Area delle Scienze 181/A, 43124 Parma, Italy

[b] Department of Civil Engineering, University of Calabria, via Pietro Bucci, 87036 Arcavacata di Rende (CS), Italy

[c] Department of Engineering, University of Naples Parthenope, Centro Direzionale Isola C4, 80143 Napoli, Italy

[d] Department of Mechanical Engineering, Faculty of Technology, University of Brasília, Campus Darcy Ribeiro, Asa Norte, Brasília, Brazil

Corresponding author: sabrina.vantadori@unipr.it

ABSTRACT

In the present paper, a criterion for fatigue assessment of high strength steels is proposed, where the influence of non-metallic inclusions on fatigue life is taken into account. To such an aim, the Carpinteri et al. criterion is used in conjunction with the $\sqrt{area}$-parameter model by Murakami and Yanase. An experimental campaign available in the literature is analysed to evaluate the criterion accuracy.

KEYWORDS: non-metallic inclusions; high strength steel; fatigue strength; infinite life; AISI 4140 steel

NOMENCLATURE

$\hat{1}\hat{2}\hat{3}$	averaged principal stress directions
C_a	amplitude of the shear stress component on the critical plane
HV	Vickers hardness
I	error index
N_a	amplitude of the normal stress component perpendicular to the critical plane
$N_{eq,a}$	equivalent normal stress amplitude on the critical plane
N_m	mean value of the normal stress component perpendicular to the critical plane
V	volume of the useful section
V_0	standard inspection volume
$\mathbf{w}$	normal vector to the critical plane
β	phase shift between normal stress and shear stress
δ	off-angle defining the normal to the critical plane
ΔK_{th}	threshold value of stress-intensity factor range
$\sigma_{af,-1}$	material fatigue strength under fully reversed normal stress
$\sigma_{eq,a}$	equivalent uniaxial stress amplitude
σ_u	material ultimate tensile strength
σ_w	fatigue limit under normal loading
σ_{wl}	lower bound of the fatigue limit under normal loading
σ_{wu}	upper bound of the fatigue limit under normal loading
$\sigma_{x,a}$	amplitude of the applied normal stress
$\tau_{af,-1}$	material fatigue strength under fully reversed shear stress

τ_w	fatigue limit under torsion
τ_{wl}	lower bound of the fatigue limit under torsion
$\tau_{xy,a}$	amplitude of the applied shear stress

1. INTRODUCTION

Non-metallic inclusions (NMIs) are naturally occurring products which are formed during both the steel production and the manufacturing/treatment processes involving the metal in a liquid state **[1]**. NMIs are chemical compounds of metals such as, for example, iron, manganese, aluminium, and silicon with non-metals such as, for example, oxygen, carbon, and hydrogen, forming separated phases in the steel matrix. When NMIs contain more than one single compound, they are named complex NMIs.

Non-metallic inclusions are one of the leading cause of failure reported in the literature, regarding gearboxes **[2-7]**, pipelines, railway wheels, crankshafts and so on **[8-12]**. Causes of premature fatigue failures related to roller element bearings in wind turbine gearboxes, ideally designed to last a lifetime of 20-25 years, are reported in the literature **[2-5,10,11]**. It is worth noting that fatigue failure counts for more than 60% of wind turbine gearbox failures, where bearing failure counts for about 70%. More precisely, it has been experimentally observed that the failure of such bearings is often associated with the occurrence of White Etching Cracks (WECs), where the crack initiation sites are in correspondence of non-metallic inclusions produced during the steel manufacturing process.

The main causes of corrosion and damage in oil- and gas-pipelines are hydrogen-induced cracking and sulphide stress cracking **[12-14]**. In more detail, the corrosion is produced by the penetration of hydrogen atoms (from the oil or gas) into the

steel which, accumulating into surface defects in steel matrix, cause the crack initiation due to the high internal pressure exerted by the formed hydrogen gas **[15-17]**. In fact, An et al. **[15]** experimentally investigated the effect of hydrogen environment on the fatigue crack growth of X80 pipeline steel, by observing that hydrogen facilitated the failure of the material in presence of defects, such as Mn_3TiSi inclusions. Therefore, non-metallic inclusions act as trapping sites to capture hydrogen **[18-20]**, and several studies on their chemical compositions have been carried out with the aim to optimise the steel processing and to reduce their presence in the metallic matrix **[21-23]**.

In rolling contact fatigue, characterising the railway wheels subjected to the cyclic rolling contact with rails, one type of crack initiation position is at the subsurface **[24-26]**. As a matter of fact, fatigue cracks may initiate and propagate from internal defects, such as non-metallic inclusions, that exist below the wheel tread surface **[27-30]**, and significant plastic deformation may be present around such inclusions, as observed by Mahdavi et al. **[31]**. Moreover, rolling contact fatigue is a key feature reducing the service lives also of wind turbine gear, for which the influence of different inclusion sizes on failure risk has been investigated by Zhou et al. **[32]**.

Numerous research studies have shown that fatigue is the dominant mechanisms for crankshaft failures **[33]**, involving both web marine crankshafts **[34]** and diesel engine crankshafts used in

commercial vehicles **[35-38]**, and that fatigue cracks are likely to initiate from non-metallic inclusions **[39,40]**.

It is worth noting that fatigue failure mostly originates at non-metallic inclusions for high strength steels, whereas it originates by the formation of persistent slip bands at grain boundaries for low/medium strength steels. Several experimental studies on high strength steels have shown that both short and long lifetimes are affected by NMIs **[41-45]**. Therefore, it seems important to consider their influence in estimating the fatigue lifetime.

To such an aim, Machado et al. **[46]** proposed to use a classical critical plane-based criterion in conjunction with the concept of the $\sqrt{area}$ -parameter by Murakami **[47]** and Yanase et al. **[48]**. Such a fatigue endurance methodology has been applied for the first time by employing both the Findley criterion **[49]** and the Modified Wöhler Curve Method (MWCM) **[50]**.

The novelty of the present paper is to implement the $\sqrt{area}$ concept in the Carpinteri et al. criterion **[51-56]**, so that the criterion can be also used to estimate the fatigue strength of naturally defective high strength steels under multiaxial loading (steels for which NMIs strongly affect lifetime).

Such an extended criterion is employed to simulate an experimental campaign available in the literature, and performed on AISI 4140 steel specimens. Moreover, the volume associated to the useful cross-section, used to estimate the maximum inclusion

size, is optimised in order to minimise the mean value of the error index.

The paper is structured as follows: the effect of non-metallic inclusions on uniaxial fatigue strength is examined in **Section 2**. **Section 3** describes the fatigue endurance methodology here proposed for multiaxial loading. In **Section 4** the available experimental campaign used to assess the proposed methodology accuracy is examined and detailed. The results determined through the above methodology are presented in **Section 5**, and the main conclusions are summarised in **Section 6**.

2. EFFECT OF NON-METALLIC INCLUSIONS ON UNIAXIAL FATIGUE STRENGTH

2.1 Basic concepts

As is well-known, when the notch depth is of the same order as the size of the fatigue damage domain at the root of the notch (this is the case of shallow notches), the classical theories cannot be applied to estimate the fatigue limit.

In such a context, Murakami et al. **[57]** performed rotating bending fatigue tests on two types of steel (i.e. a low carbon and a medium carbon steel), by using specimens containing small artificial holes of different diameters (between 40 and 200 μm). They observed the presence of non-propagating cracks in all specimens at fatigue limit (that is, at the maximum nominal stress for which the life was at least 10^7 loading cycles), concluding that fatigue limit was the threshold condition for non-propagation

of cracks emanating from holes. Moreover, they observed that there were non-damaging defects, which did not decrease the fatigue strength. Thus, this study not only revealed that a critical defect size seemed to exist, but also that the size of the defect was crucial to determine the fatigue strength, mainly in high strength metals **[57,58]**.

Therefore, it was recognised that the fatigue problem involving components with small defects could also be treated as a short crack problem, where the fatigue limit concept is associated with the presence of dormant cracks, and modified Stress Intensity Factor (SIF) based methodologies could be considered to tackle the problem.

The maximum value of the SIF along the front of a 3D crack has a strong correlation with the square root of the cracked area, $\sqrt{area}$ **[59]**, such a parameter being defined as the square root of the area determined by projecting the crack into the plane perpendicular to the maximum principal stress.

Murakami analysed fatigue limit results under rotating bending tests and tension-compression tests, performed on specimens made of ten different materials, containing very small drilled holes, very small and shallow notches, and very shallow circumferential cracks. The aim was to correlate the threshold value ΔK_{th} of stress-intensity factor range with the $\sqrt{area}$, where the $\sqrt{area}$ was the projection of the above small defects and cracks into the plane perpendicular to the maximum principal stress **[60]**. The

Authors of such a paper found a linear relationship between ΔK_{th} and $\sqrt{area}$ in a logarithmic scale, with slope equal to $1/3$:

$$\Delta K_{th} \propto \left(\sqrt{area}\right)^{\frac{1}{3}} \tag{1}$$

where ΔK_{th} was computed according to the relationship for the maximum value of the SIF along the front of a 3D surface crack **[59]**:

$$\Delta K_{th} = 0.65\left(2\sigma_w\right)\sqrt{\pi\sqrt{area}} \tag{2}$$

being σ_w the fatigue limit expressed in MPa, ΔK_{th} in MPa$\sqrt{\text{m}}$ and $\sqrt{area}$ in μm. Moreover, the Authors observed that materials having higher Vickers hardness, HV, showed highest values of ΔK_{th}, and the relationship between ΔK_{th} and HV could be expressed by:

$$\Delta K_{th} \propto \left(HV + C\right) \tag{3}$$

being C a material independent constant.

By combining Eq. (1) with Eq. (3) and by applying the least squares method, ΔK_{th} could be expressed as follows:

$$\Delta K_{th} = 3.3\left(10\right)^{-3}\left(HV + 120\right)\left(\sqrt{area}\right)^{\frac{1}{3}} \tag{4}$$

with $\sqrt{area}$ in μm, HV in kgf/mm^2. By employing Eq. (2), the fatigue limit was given by:

$$\sigma_w = \frac{1.43(HV+120)}{\left(\sqrt{area}\right)^{\frac{1}{6}}} \tag{5}$$

2.2 Fatigue strength estimation equation under normal loading: the $\sqrt{area}$ -parameter model

The fatigue fracture origin in low/medium strength steels is different from that in high strength steels.

Slip bands and/or grain boundary cracks, that nucleate in the matrix, represent the fatigue fracture origins typical of low/medium strength steels. In such a case, the size of inclusions, generally formed during the production process, are smaller than a critical value. The following linear empirical equation holds:

$$\sigma_w = 1.6HV \tag{6}$$

where σ_w is expressed in MPa and HV in kgf/mm^2.

White spots (or fish eyes), in the vicinity of non-metallic inclusions and in the form of white circular areas on the fracture surface, represent the fatigue fracture origins typical of high strength steels, where the fatigue crack: (a) nucleates at the

interface between the inclusion and the matrix and/or the inclusion itself is cracked, (b) propagates by a small amount, and (c) then stops propagating. In such a case, the relationship between fatigue limit and hardness, given by Eq. (6), is no longer valid since σ_w depends on the hardness of the microstructure close to the fracture origin and not on the average hardness. Moreover, it was experimentally observed that the σ_w values fell below the straight line represented by Eq. (6), and a large scatter was registered by varying HV **[47,61]**.

It is worth noting that, when the crack nucleates, the stress within the inclusion is relieved, and the inclusion may be regarded as mechanically equivalent to a small defect. In such a case which is typical of high strength steels, the sizes of inclusions, generally formed during heat treatment, are greater than a critical value. The non-metallic inclusions can be treated as small defects, where Eq. (5) holds for a surface inclusion, whereas the coefficient 1.43 in Eq. (5) is replaced by either 1.41 for an inclusion just in contact with the free surface or 1.56 for an internal inclusion.

Note that $\sqrt{area}$ in Eq.(5) is the square root of the "area" of an inclusion into a plane perpendicular to the maximum principal stress.

Therefore, low cycle fatigue limit values in high strength steels are due to the presence of inclusions larger than a critical size and, since both the location and sizes of inclusions

influence the σ_w value, a wide scatter band of the experimental data was observed **[47,61]**.

Due to the fact that inclusions are more than a single one, it is needed to consider a statistical distribution of the inclusions, providing for σ_w not a unique value but an upper and a lower bound. The upper bound is provided by Eq.(6), which holds when inclusions do not affect σ_w ($\sigma_{wu} = 1.6HV$). The lower bound is computed by assuming that: (i) the inclusion with the maximum area, $area_{max}$, contained in the selected cross-section of the specimen is expected to become the fatigue fracture origin, and (ii) such an inclusion is just below the cross-section surface. Such a lower bound is given by:

$$\sigma_{wl} = \frac{1.44\left(HV + 120\right)}{\left(\sqrt{area}_{max}\right)^{\frac{1}{6}}} \tag{7}$$

Different methods are available in the literature to estimate $\sqrt{area}_{max}$. According to Murakami **[47]**, such a fatigue strength for high strength steels can be assumed to occur in correspondence of $1 \cdot (10)^7$ loading cycles.

2.3 Fatigue strength estimation equation under shear loading: the $\sqrt{area}$-parameter model

In view of Eq.(5), Yanase et al. **[48]** proposed a simple yet reasonably accurate equation to estimate fatigue limit under torsion:

$$\tau_w = \frac{1.21\left(HV + 120\right)}{\left(\sqrt{area}\right)^{\frac{1}{6}}} \tag{8}$$

Therefore, according to (i) and (ii) assumptions above, the torsion fatigue limit is given by:

$$\tau_{wl} = \frac{1.19\left(HV + 120\right)}{\left(\sqrt{area}_{max}\right)^{\frac{1}{6}}} \tag{9}$$

where such an equation is simply obtained from Eq.(8) by replacing $\sqrt{area}$ with $\sqrt{1.137} \cdot \sqrt{area}_{max}$.

3. MULTIAXIAL FATIGUE STRENGTH ESTIMATION: THE CARPINTERI CRITERION COUPLED WITH THE $\sqrt{area}$ -PARAMETER MODEL

The criterion proposed by Carpinteri et al. **[51-56]** uses the following non-linear relationship to assess the fatigue damage:

$$\sigma_{eq,a} = \sqrt{N_{eq,a}^2 + \left(\frac{\sigma_{af,-1}}{\tau_{af,-1}}\right)^2 C_a^2} \le \sigma_{af,-1} \tag{10}$$

where $\sigma_{af,-1}$ and $\tau_{af,-1}$ are the fatigue strengths (at a given number of loading cycles, N_0, generally assumed equal to $2\cdot(10)^6$) for fully reversed normal stress and for fully reversed shear stress, respectively. The values $N_{eq,a}$ and C_a are computed on the critical plane, where its normal **w** is defined by means of both the direction $\hat{1}$ of maximum principal stress, at the time instant when such a stress attains its maximum value, and the angle δ given by:

$$\delta = \frac{3}{2}\left[1-\left(\frac{\tau_{af,-1}}{\sigma_{af,-1}}\right)^2\right]45° \tag{11}$$

More precisely, the $\hat{1}$ direction is rotated by δ in the $\hat{1}\hat{3}$ plane **[51-56]**. The value of $N_{eq,a}$ is computed as follows:

$$N_{eq,a} = N_a + \sigma_{af,-1}\left(\frac{N_m}{\sigma_u}\right) \tag{12}$$

where σ_u is the ultimate tensile strength of the material, N_a and N_m are the amplitude and the mean value of the stress normal to the critical plane, respectively. The value of C_a, which is the amplitude of the shear stress lying on the critical plane, is computed according to the Maximum Rectangular Hull method **[62]**.

Since the aim of the present work is the coupling of the above multiaxial criterion with the $\sqrt{area}$-parameter model (outlined in **Section 2.2** and **2.3**), the fatigue strengths $\sigma_{af,-1}$ and $\tau_{af,-1}$ in Eqs (10-12) are replaced with σ_{wl} and τ_{wl}, respectively. In such a way, the Carpinteri et al. criterion can be used to also estimate the fatigue strength of naturally defective high strength steels under multiaxial loading, which are steels for which NMIs strongly affect lifetime.

4. EXPERIMENTAL WORK EXAMINED

4.1 Multiaxial fatigue testing

The experimental campaign here examined is available in the literature **[46,63,64]**.

The specimens were cut from a broken power generator crankshaft which had experienced failure under service. The material was AISI 4140 steel, oil quenched and tempered at 600°C, whose mechanical properties are listed in **Table 1**.

Table 1

The specimen manufacturing process consisted of cutting prisms from the block of the crankshaft material. That was followed by machining such prisms to the designed specimen geometry, shown in **Figure 1**, and then polishing the specimens with sandpaper to a final roughness lower than $0.2\mu m$.

Figure 1

The fatigue tests were performed under load control according to the international standard ASTM E466-15, by using a servo-hydraulic axial-torsional fatigue testing machine (100 kN and 1100 Nm load capacity, respectively). Fully reversed sinusoidal signals were considered. Test frequencies were between 5 and 15 Hz, depending on the loading level. The values of the ratio between shear stress amplitude $\tau_{xy,a}$ and normal stress amplitude $\sigma_{x,a}$ were (a) 0.0, 0.5, 1.0, 2.0 and ∞ with a phase shift β equal to 0°, and (b) 0.5, 1.0 and 2.0 with a phase shift $\beta = 90°$ **[46,63,64]**. Two tests were performed for each loading condition.

The specimen complete rupture was used as the failure criterion, whereas the run-out condition was in correspondence of $2 \cdot (10)^6$ loading cycles.

Under uniaxial loading, the S-N (normal stress against number of loading cycles) and T-N (shear stress against number of loading cycles) curves obtained were expressed by:

$$S = 1202 N^{-0.083} \tag{13}$$

$$T = 679 N^{-0.062} \tag{14}$$

with S and T in MPa and N is the number of loading cycles.

The results obtained under multiaxial loading are reported in detail in Ref. **[46]**.

4.2 Estimation of the maximum inclusion size $\sqrt{area}_{\max}$

In order to compute σ_{wl} (see Eq.(7)) and τ_{wl} (see Eq.(9)), an inclusion content analysis was performed **[46,63,64]**, and the main steps and results are here reported.

Two cross-sections of a specimen (described in **Section 4.1**) were examined: one is perpendicular to the longitudinal axis of the specimen (representing the direction of the maximum principal stress under fully reversed axial loading), and the other one is forming 45° with the longitudinal axis of the specimen. Each cross-section was observed by a Scanning Electron Microscope (SEM, JEOL JSM-7100F) with an inspection area equal to $0.41mm^2$ (standard inspection area); the biggest inclusion was identified and its area was computed as that enclosed by a smooth bounder line surrounding the inclusion; then, the value of $\sqrt{area}_{max,i}$ was obtained. Such an operation was repeated 60 times for each cross-section ($i=1,...60$).

Then, the trend of a reduced variable y against the variable $\sqrt{area}_{max}$ was plotted, and the following inclusion distributions were computed:

$$\sqrt{area}_{max}=\frac{1}{0.0963}y+\frac{1.0671}{0.0963} \tag{15}$$

for the cross-section perpendicular to the longitudinal axis of the specimen, and:

$$\sqrt{area}_{max} = \frac{1}{0.1184} y + \frac{1.4751}{0.1184} \tag{16}$$

for the cross-section forming an angle equal to 45° with respect to the above axis, with the reduced variable y given by:

$$y = -ln\left[-ln\left(\frac{T-1}{T}\right)\right] \tag{17}$$

being T the return period.

In order to compute T, two volumes have to be identified:

$$T = \frac{V}{V_0} \tag{18}$$

where V is the volume associated to the useful cross-section, whereas V_0 is the standard inspection volume, computed as the product of the inspection area, S_0, and the thickness of the observed cross-section by SEM, h. V was set equal to the volume of the specimen gauge region, that is, $V_1 = 2400 mm^3$, whereas V_0 was computed by using the data coming from the microscope observations, that is, equal to 0.00617mm^3 for the cross-section perpendicular to the longitudinal axis of the specimen ($S_0 = 0.41 mm^2$, $h = 1.51(10)^{-2} mm$) and 0.00643mm^3 for the cross-section forming an angle equal to 45° with respect to the above axis ($S_0 = 0.41 mm^2$, $h = 1.57(10)^{-2} mm$). More details may be found in Ref. **[46]**. It is

worth noting that, by increasing V, the probability to find bigger inclusions within this volume increases.

The computed values of $\sqrt{area}_{max}$ were $145\mu m$ and $121\mu m$ for the cross-sections perpendicular to and forming an angle of 45° with the longitudinal axis of the specimen, respectively.

4.3 Fatigue strength affected by non-metallic inclusions

By employing Eqs (7) and (9), the fatigue strength σ_{wl} was equal to 271MPa, whereas τ_{wl} was equal to 235MPa.

Since the run-out condition in the experimental campaign examined was taken in correspondence of $2\cdot(10)^6$ loading cycles, it was assumed that the fatigue strength affected by non-metallic inclusions could be estimated at $2\cdot(10)^6$. Therefore, assuming the same slopes of the experimental S-N and T-N curves reported in Eqs (13) and (14), the new values of σ_{wl} and τ_{wl}, corresponding to $2\cdot(10)^6$ cycles were equal to 309MPa and 260MPa, respectively.

5. RESULTS

5.1 Uniaxial and multiaxial fatigue results

The multiaxial criterion outlined in **Section 3** is applied to simulate uniaxial and multiaxial fatigue tests, where $\sigma_{af,-1}=\sigma_{wl}$ and $\tau_{af,-1}=\tau_{wl}$.

More precisely, Eq.(10) is graphically represented by an ellipse in the C_a against $N_{eq,a}$ diagram (**Figure 2**). Fatigue failure occurs if the point associated with a given experimental test lies out of the elliptical domain, whereas the safe points are those located inside such a domain.

Figure 2

In **Figure 2**, the error band equal to $\pm 10\%$ is represented by dashed lines, whereas that equal to $\pm 20\%$ is represented by dash-dot lines. The full symbols refer to specimens that failed, whereas the empty ones refer to run-outs. Moreover, empty symbols in red represent loading conditions in correspondence of which both failure and run-out were experimentally observed. The in-phase loading conditions are plotted in **Figure 2(a)**, whereas the out-of-phase loading conditions are plotted in **Figure 2(b)**.

The following remarks can be outlined from **Figure 2(a)**:

- under fully reversed axial loading (that is, $\frac{\tau_{xy,a}}{\sigma_{x,a}} = 0$), the criterion estimates the failure of all test specimens, that is, the results are too conservative although most of the results falls into the $+20\%$ scatter band;
- under fully reversed torsion loading (that is, $\frac{\tau_{xy,a}}{\sigma_{x,a}} = \infty$), the estimation are in complete agreement with the experimental results;

- under multiaxial loading, although the criterion is generally not able to correctly capture failure and run-out conditions, it provides conservative estimates, being the above points out or very close to the elliptical domain.

The following remarks can be outlined from **Figure 2(b)**:

- under multiaxial loading and $\frac{\tau_{xy,a}}{\sigma_{x,a}} = 0.5$, the estimations (except one) are in agreement with the experimental data;
- under multiaxial loading and $\frac{\tau_{xy,a}}{\sigma_{x,a}} = 1.0$ or $\frac{\tau_{xy,a}}{\sigma_{x,a}} = 2.0$, the estimations are totally in agreement with the experimental data.

The accuracy of the criterion is evaluated through the error index, I, given by:

$$I = \frac{\sigma_{eq,a} - \sigma_{af,-1}}{\sigma_{af,-1}} \cdot 100 \tag{19}$$

The mean value $\bar{I}$ of the error index is equal to 1.4% for all loading conditions examined. A comparison in terms of $\bar{I}$ is performed applying the Findley criterion **[49]** and the MWCM **[50]**, by separating the computation for in-phase loading from that for out-of-phase loading, as is listed in **Table 2**. The comparison shows that a more satisfactory accuracy is obtained by applying the Carpinteri et al. criterion, being the $|\bar{I}|$ value lower than 10% for both in- and out-of-phase loading.

Table 2

5.2 Optimisation of the volume associated to the useful section

As is described in **Section 4.2**, the value of the volume V has to be set. Different values of V are considered and listed in **Table 3**: $V_2 = 10V_1$, $V_3 = 30V_1$, and V_4 equal to the crankshaft volume, where $V_1 = 2400mm^3$ is the volume employed in **Section 5.1**.

Table 3

By performing the aforementioned procedure (**Section 5.1**) for each volume value above, the mean value of I is computed and listed in **Table 3** together with the corresponding values of σ_{wl} and τ_{wl}.

The procedure is also repeated by using the experimental values of the fatigue strength under both fully reversed axial loading (equal to 375 MPa **[46]**) and fully reversed torsion loading (equal to 282MPa **[46]**). The mean value of I is computed and listed in **Table 3**.

For all the above cases, the $C_a - N_{eq,a}$ plots are shown in **Figures** from **3** to **6**.

Figure 3

Figure 4

Figure 5

Figure 6

In **Figure 7**, $\bar{I}$ (the mean value of I) is plotted against σ_{wl}. Such points can be interpolated by a parabolic curve:

$$\bar{I} = 250.62 - 1.31\sigma_{wl} + 0.016\sigma_{wl}^2 \qquad (20)$$

where $\bar{I}$ is equal to zero when $\sigma_{wl} = 313MPa$, value assumed in correspondence of $2\cdot(10)^6$ loading cycles (**Figure 7**). The corresponding value of σ_{wl} at $1\cdot(10)^7$ cycles is equal to 274MPa.

Figure 7

By exploiting Eq.(7), the value of $\sqrt{area}_{max}$ results to be equal to $135.16\mu m$ and, consequently, the values of y (by Eq.(15), $y = 11.95$) and T (by Eq.(17), $T = 154649.85$) can be computed. Then, by employing Eq.(18), the value of the 'optimum' volume associated to the useful cross-section that determines $\bar{I} = 0$ can be computed: $V_{opt} = 954.19mm^3$.

The value of τ_{wl} for such a return period is computed: it is equal to 238MPa at $1\cdot(10)^7$ loading cycles, and 263MPa at $2\cdot(10)^6$ loading cycles.

By employing the values of fatigue strength at $2\cdot(10)^6$ cycles, that is, $\sigma_{wl}=313MPa$ and $\tau_{wl}=263MPa$ in Eq.(10), the results obtained by applying the multiaxial criterion by Carpinteri et al. in conjunction with the $\sqrt{area}$-parameter model by Murakami and Yanase are shown in **Figure 8**.

Figure 8

6. CONCLUSIONS

In the present paper, the authors have proposed to extend the Carpinteri et al. criterion to fatigue assessment of high strength steels characterised by a fatigue life strongly influenced by non-metallic inclusions.

To such an aim, the above multiaxial criterion has been used in conjunction with the $\sqrt{area}$ concepts proposed by Murakami and Yanase.

The extended criterion has been applied to an experimental campaign available in the literature and performed on AISI 4140 steel specimens.

The results have been quite satisfactory, being the criterion accuracy higher than that of two other criteria available in the literature.

On the basis of such results, it has been observed that the volume of the specimen gauge-length region is suitable, since a very low value of $\bar{I}$ is obtained. Moreover, an optimisation

procedure has been employed in order to find the volume corresponding to the error index mean value equal to zero.

Acknowledgements

The research work of Sabrina Vantadori and Andrea Zanichelli is supported by Italian Ministry of University and Research (P.R.I.N. National Grant 2017, Project code 2017HFPKZY; University of Parma Research Unit).

J.A. Araújo is also grateful for the support provided by CNPq (contract 305302/2017-5). This study was financed in part by the Coordenação de Aperfeiçoamento de Pessoal de Nível Superior - Brasil (CAPES) - Finance Code 001 and by Fundação de Amparo a Pesquisa do Distrito Federal – FAP-DF.

REFERENCES

[1] Kiessling R., Lange N., Non-metallic inclusions in steel. London, UK: Metals Society; 1978. ISBN 090435718X 9780904357189

[2] Bruce T., Long H., Slatter T., Dwyer-Joyce R.S., Formation of white etching cracks at manganese sulfide (MnS) inclusions in bearing steel due to hammering impact loading. Wind Energy, 2016; 19: 1903-1915. DOI 10.1002/we.1958

[3] Evans M.-H., An updated review: white etching cracks (WECs) and axial cracks in wind turbine gearbox bearings. Materials Science and Technology (United Kingdom), 2016; 32: 1133-1169. DOI 10.1080/02670836.2015.1133022

[4] Al-Tameemi H.A., Long H., Dwyer-Joyce R.S., Initiation of sub-surface micro-cracks and white etching areas from debonding at non-metallic inclusions in wind turbine gearbox bearing. Wear, 2018; 406-407: 22-32. DOI 10.1016/j.wear.2018.03.008

[5] Al-Tameemi H.A., Long H., Finite element simulation of subsurface initiated damage from non-metallic inclusions in wind turbine gearbox bearings. International Journal of Fatigue, 2020; 131: 105347. DOI 10.1016/j.ijfatigue.2019.105347

[6] Feng W., Feng Z., Mao L., Failure analysis of a secondary driving helical gear in transmission of electric vehicle. Engineering Failure Analysis, 2020; 117: 104934. DOI 10.1016/j.engfailanal.2020.104934

[7] Kishore K., Sharma A., Mukhopadhyay G., Failure Analysis of a Gearbox of a Conveyor Belt. Journal of Failure Analysis and Prevention, 2020; 20, 4: 1237-1243. DOI 10.1007/s11668-020-00928-4

[8] Sun K., Sun Q., Zhang Y., Shi B., Zhao B., A pragmatic approach to predict fatigue strength concerning the short crack behavior in VHCF. International Journal of Fatigue, 2020; 135: 105561. DOI 10.1016/j.ijfatigue.2020.105561

[9] Boulifa M.I., Hadji A., Study of the influence of alloying elements on the mechanical characteristics and wear behavior of a ductile cast iron. Frattura ed Integrità Strutturale, 2021; 56: 74-83. DOI 10.3221/IGF-ESIS.56.06

[10] Liu R., Sun D., Hou J., Liu F., Li Q., Fatigue life analysis of wind turbine gear with oxide inclusion. Fatigue and Fracture of Engineering Materials and Structures, 2021; 44: 776-787. DOI 10.1111/ffe.13393

[11] López-Uruñuela F.J., Fernández-Díaz B., Pagano F., López-Ortega A., Pinedo B., Bayón R., Aguirrebeitia J., Broad review of "White Etching Crack" failure in wind turbine gearbox bearings: Main factors and experimental investigations. International Journal of Fatigue, 2021; 145: 106091. DOI 10.1016/j.ijfatigue.2020.106091

[12] Doglione R., Firrao D., Structural collapse calculations of old pipelines. International Journal of Fatigue, 1998; 20: 161-168. DOI 10.1016/S0142-1123(97)00100-X

[13] Chapetti M.D., Otegui J.L., Motylicki J., Fatigue assessment of an electrical resistance welded oil pipeline. International Journal of Fatigue, 2002; 24: 21-28. DOI 10.1016/S0142-1123(01)00111-6

[14] Amezhnov A.V., Rodionova I.G., Effect of Non-Metallic Inclusion Chemical and Phase Composition on Corrosion Resistance of Carbon and Low Alloy Steels in Water Media Typical for Oilfield Pipeline Operating Conditions. Metallurgist, 2019; 63: 717-726. DOI 10.1007/s11015-019-00881-0

[15] An T., Zhang S., Feng M., Luo B., Zheng S., Chen L., Zhang L., Synergistic action of hydrogen gas and weld defects on fracture toughness of X80 pipeline steel. International Journal of Fatigue, 2019; 120: 23-32. DOI 10.1016/j.ijfatigue.2018.10.021

[16] Muthanna B.G.N., Bouledroua O., Meriem-Benziane M., Hadj-Meliani M., Pluvinage G., Suleiman R.K., Numerical study of semi-elliptical cracks in the critical position of pipe elbow. Frattura ed Integrità Strutturale, 2019; 13: 463-477. DOI 10.3221/IGF-ESIS.49.44

[17] Zerbst U., Klinger C., Material defects as cause for the fatigue failure of metallic components. International Journal of Fatigue, 2019; 127: 312-323. DOI 10.1016/j.ijfatigue.2019.06.024

[18] Belaïd M., Malika M., Mokadem S., Boualem S., Probabilistic elastic-plastic fracture mechanics analysis of propagation of cracks in pipes under internal pressure. Frattura ed Integrità Strutturale, 2020, 14; 202-210. DOI 10.3221/IGF-ESIS.54.15

[19] Kryzhanivskyi E.I., Nykyforchyn H.M., Student O.Z., Krechkovska H.V., Chudyk I.I., Role of Nonmetallic Inclusions in Premature Stress-Corrosion Fractures of Drill Pipes. Materials Science, 2020; 55: 822-830. DOI 10.1007/s11003-020-00375-4

[20] Makarenko V.D., Fedorina T.P., Bezpala O.V., Maksimov S.Yu., The influence of the pipelines operation term in aggressive environments on the gas content and structure of structural steels. Solid State Phenomena, 2021; 313: 136-142. DOI 10.4028/www.scientific.net/SSP.313.136

[21] Ren Q., Zhang Y., Ren Y., Zhang L., Wang J., Wang Y., Prediction of spatial distribution of the composition of inclusions on the entire cross section of a linepipe steel continuous casting slab. Journal of Materials Science and Technology, 2021; 61: 147-158. DOI 10.1016/j.jmst.2020.05.035

[22] Shaposhnikov N., Ermakov B., Zhukov N., Fedorov A., Analysis of the reasons for the accelerated failure of oil pipelines in the regions of the Far North and Siberia. E3S Web of Conferences, 2021; 225, 06001. DOI 10.1051/e3sconf/202122506001

[23] Shapovalov A.N., Dema R.R., Nefed'ev S.P., Experience of using complex modifiers to increase corrosion resistance of pipe steels. Solid State Phenomena, 2021; 316 SSP: 369-374. ISBN 978-303573650-2

[24] Kawiak M., Balitskii A., Embrittlement of welded joints of tram rails in city environments. Engineering Failure Analysis, 2018; 85: 97-103. DOI 10.1016/j.engfailanal.2017.12.011

[25] Cao Z., Shi Z., Yu F., Wu G., Cao W., Weng Y., A new proposed Weibull distribution of inclusion size and its correlation with rolling contact fatigue life of an extra clean bearing steel. International Journal of Fatigue, 2019; 126: 1-5. DOI 10.1016/j.ijfatigue.2019.04.031

[26] Mahdavi H., Poulios K., Niordson C.F., Effect of superimposed compressive stresses on rolling contact fatigue initiation at hard and soft inclusions. International Journal of Fatigue, 2020; 134, 105399. DOI 10.1016/j.ijfatigue.2019.105399

[27] Oezel M., Janitzky T., Beiss P., Broeckmann C., Influence of steel cleanliness and heat treatment conditions on rolling contact fatigue of 100Cr6. Wear, 2019; 430-431: 272-279. DOI 10.1016/j.wear.2019.04.026

[28] Masoudi Nejad R., Farhangdoost K., Shariati M., Microstructural analysis and fatigue fracture behavior of rail steel. Mechanics of Advanced Materials and Structures, 2020; 27: 152-164. DOI 10.1080/15376494.2018.1472339

[29] Protopopov E.V., Chislavlev V.V., Temlyantsev M.V., Golovatenko A.V., Increasing the Efficiency of Refining Rail Steel in Intermediate CCM Ladles Based on Rational Organization of Hydrodynamic Processes. Steel in Translation, 2020; 50: 283-288. DOI 10.3103/S0967091220050101

[30] Kato T., Fujimura T., Hiramatsu S., Yamamoto Y., Subsurface crack propagation from internal defect in rolling contact fatigue of railway wheel steel. Materials Transactions, 2021; 62, 2: 185-190. DOI 10.2320/matertrans.Z-M2020860

[32] Mahdavi H., Poulios K., Kadin Y., Niordson C.F., Finite element study of cyclic plasticity near a subsurface inclusion under rolling contact and macro-residual stresses. International Journal of Fatigue, 2021; 143: 105981. DOI 10.1016/j.ijfatigue.2020.105981

[32] Zhou H., Wei P., Liu H., Zhu C., Lu C., Deng G., Roles of microstructure, inclusion, and surface roughness on rolling contact fatigue of a wind turbine gear. Fatigue and Fracture of Engineering Materials and Structures, 2020; 43, 7: 1368-1383. DOI 10.1111/ffe.13199

[33] Moore D.A., Packer K.F., Jones A.J., Carlson D.M., Crankshaft failure and why it may happen again. Journal of Failure Analysis and Prevention, 2001; 1: 63-72. DOI 10.1007/bf02715199

[34] Fonte M., de Freitas M., Marine main engine crankshaft failure analysis: A case study. Engineering Failure Analysis, 2009; 16: 1940-1947. DOI 10.1016/j.engfailanal.2008.10.013

[35] Bai S., Hu Y., Zhang H., Zhou S., Jia Y., Li G., Failure analysis of commercial vehicle crankshaft: A case study. Applied Mechanics and Materials, 2012; 192: 78-82. DOI 10.4028/www.scientific.net/AMM.192.78

[36] Liu C.Z., Hao Y.G., Chen X.F., Li X.D., Fracture analysis of a crankshaft used for heavy-duty truck. Applied Mechanics and Materials, 2014; 654: 61-64. DOI 10.4028/www.scientific.net/AMM.654.61

[37] Aliakbari K., Failure analysis of four-cylinder diesel engine crankshaft. Journal of the Brazilian Society of Mechanical Sciences and Engineering, 2019; 41: 30. DOI 10.1007/s40430-018-1536-3

[38] Lu J.-L., Cheng G.-G., Wu M., Yang G., Che J.-L., Detection and analysis of magnetic particle testing defects on heavy truck crankshaft manufactured by microalloyed medium-carbon forging steel. Journal of Iron and Steel Research International, 2020; 27: 608-616. DOI 10.1007/s42243-019-00334-7

[39] Yakura R., Matsuda M., Sakai T., Ueno A., Effect of inclusion size on fatigue properties in very high cycle region of low alloy steel used for solid-type crankshaft. R and D: Research and Development Kobe Steel Engineering Reports, 2016; 66: 20-24.

[40] Khameneh M.J., Azadi M., Evaluation of high-cycle bending fatigue and fracture behaviors in EN-GJS700-2 ductile cast iron of crankshafts. Engineering Failure Analysis, 2018; 85: 189-200. DOI 10.1016/j.engfailanal.2017.12.017

[41] Tanaka K., Akiniwa Y., Fatigue crack propagation behaviour derived from S-N data in very high cycle regime. Fatigue & Fracture of Engineering Materials & Structures, 2002; 25: 775–84. DOI 10.1046/j.1460-2695.2002.00547.x

[42] Akiniwa Y., Miyamoto N., Tsuru H., Tanaka K., Notch effect on fatigue strength reduction of bearing steel in the very high cycle

regime. International Journal of Fatigue, 2006; 28: 1555–1565. DOI 10.1016/j.ijfatigue.2005.04.017

[43] Shiozawa K., Hasegawa T., Kashiwagi Y., Lu L., Very high cycle fatigue properties of bearing steel under axial loading condition. International Journal of Fatigue, 2009; 31: 880-888. DOI 10.1016/j.ijfatigue.2008.11.001

[44] Lambrighs K., Verpoest I., Verlinden B., Wevers M., Influence of non-metallic inclusions on the fatigue properties of heavily cold drawn steel wires. Procedia Engineering, 2010; 2: 173–181. DOI 10.1016/j.proeng.2010.03.019

[45] Shiozawa K., Murai M., Shimatani Y., Yoshimoto T., Transition of fatigue failure mode of Ni-Cr-Mo low alloy steel in very high cycle regime. International Journal of Fatigue, 2010; 32: 541-550. DOI 10.1016/j.ijfatigue.2009.06.011

[46] Machado P.V.S., Araújo L.C., Soares M.V., Araújo J.A., Multiaxial fatigue assessment of steels with non-metallic inclusions by means of adapted critical plane criteria. Theoretical and Applied Fracture Mechanics, 2020; 108: 102585. DOI 10.1016/j.tafmec.2020.102585

[47] Murakami Y., Metal Fatigue: Effects of Small Defects and Nonmetallic Inclusions. Oxford, UK: Elsevier Science Ltd.; 2002. ISBN 9780128138762

[48] Yanase K., Endo M., Multiaxial high cycle fatigue threshold with small defects and cracks. Engineering Fracture Mechanics, 2014; 123: 182–196. DOI 10.1016/j.engfracmech.2014.03.017

[49] Findley W.N., A theory for the effect of mean stress on fatigue of metals under combined torsion and axial load or bending. Journal of Engineering for Industry, 1959; 81, 4: 301–306. DOI 10.1115/1.4008327

[50] Susmel L., Lazzarin P., A bi-parametric Wöhler curve for high cycle multiaxial fatigue assessment. Fatigue & Fracture of Engineering Materials & Structures, 2002; 25: 63–78. DOI 10.1046/j.1460-2695.2002.00462.x

[51] Carpinteri A., Ronchei C., Scorza D., Vantadori S., Critical Plane Orientation Influence on Multiaxial High-Cycle Fatigue

Assessment. Physical Mesomechanics, 2015; 18: 348-354. DOI 10.1134/S1029959915040074

[52] Kurek M., Łagoda T., Carpinteri A., Vantadori S., Estimation of fatigue strength under multiaxial cyclic loading by varying the critical plane orientation. Frattura ed Integrità Strutturale, 2016; 10: 221-227. DOI 10.3221/IGF-ESIS.37.29

[53] Carpinteri A., Kurek M., Łagoda T., Vantadori S., Estimation of fatigue life under multiaxial loading by varying the critical plane orientation. International Journal of Fatigue, 2017: 100; 512-520. DOI 10.1016/j.ijfatigue.2016.10.028

[54] Vantadori S., Ronchei C., Carpinteri A., Multiaxial fatigue life evaluation of notched structural components: An analytical approach. Material Design and Processing Communications, 2019; 1, 4: e74. DOI 10.1002/mdp2.74

[55] Vantadori S., Carpinteri A., Luciano R., Ronchei C., Scorza D., Zanichelli A., Okamoto Y., Saito S., Itoh T., Crack initiation and life estimation for 316 and 430 stainless steel specimens by means of a critical plane approach. International Journal of Fatigue, 2020; 138: 105677. DOI 10.1016/j.ijfatigue.2020.105677

[56] Ronchei C., Vantadori S., Notch fatigue life estimation of Ti-6Al-4V. Engineering Failure Analysis, 2021; 120: 105098. DOI 10.1016/j.engfailanal.2020.105098

[57] Murakami Y., Fukuda S., Endo T., Effect of Micro-hole on Fatigue Strength 1st Report, Effect of Micro-hole : Dia. : 40 / 50 / 80 / 100 & 200μm) on the Fatigue Strength of 0.13% and 0.46% Carbon Steels. Transactions of the Japan Society of Mechanical Engineers Series I, 1978; 44: 4003-4013. DOI 10.1299/kikai1938.44.4003

[58] Murakami Y., Endo M., A Geometrical Parameter for the Quantitative Estimation of the Effects of Small Defects on Fatigue Strength of Metals. Transactions of the Japan Society of Mechanical Engineers Series A, 1983; 49, 438: 127-136. DOI 10.1299/kikaia.49.127

[59] Murakami Y., Kodama S., Konuma S., Quantitative Evaluation of Effects of Nonmetallic Inclusions on Fatigue Strength of High

Strength Steel. Transactions of the Japan Society of Mechanical Engineers Series A, 1988; 54, 500: 688-696. DOI 10.1299/kikaia.54.688

[60] Murakami Y., Endo M., Effects of hardness and crack geometry on ΔK_{th} of small cracks. Journal of The Society of Materials Science, Japan, 1986; 35, 395: 911-917. DOI 10.2472/jsms.35.911

[61] Saito M., Ito Y., Some Properties of Ultra Clean Spring Steel. Transactions of Japan Society of Spring Engineers, 1985; 30: 11-19. DOI 10.5346/trbane.1985.11

[62] Araújo J.A., Dantas A.P., Castro F.C., Mamiya E.N., Ferreira J.L.A., On the characterization of the critical plane with a simple and fast alternative measure of the shear stress amplitude in multiaxial fatigue. International Journal of Fatigue, 2011; 33: 1092–1100. DOI 10.1016/j.ijfatigue.2011.01.002

[63] Araújo L.C., Machado P.V.S., Pereira M.V.S., Araújo J.A., An alternative approach to calibrate multiaxial fatigue models of steels with small defects. Procedia Structural Integrity, 2019; 19: 19-26. DOI 10.1016/j.prostr.2019.12.004

[64] Machado P.V.S., Araújo L.C., Soares M.V., Araújo J.A., The use of a modified critical plane model to assess multiaxial fatigue of steels with nonmetallic inclusion. MATEC Web of Conferences, 2019; 300: 16005. DOI 10.1051/matecconf/201930016005

INFLUENCE OF NON-METALLIC INCLUSIONS ON THE HIGH CYCLE FATIGUE STRENGTH OF STEELS

Sabrina Vantadori[a*], Camilla Ronchei[b], Daniela Scorza[c], Andrea Zanichelli[a], Lucas Carneiro Araújo[d], José Alexander Araújo[d]

[a] Department of Engineering & Architecture, University of Parma, Parco Area delle Scienze 181/A, 43124 Parma, Italy

[b] Department of Civil Engineering, University of Calabria, via Pietro Bucci, 87036 Arcavacata di Rende (CS), Italy

[c] Department of Engineering, University of Naples Parthenope, Centro Direzionale Isola C4, 80143 Napoli, Italy

[d] Department of Mechanical Engineering, Faculty of Technology, University of Brasília, Campus Darcy Ribeiro, Asa Norte, Brasília, Brazil

Corresponding author: sabrina.vantadori@unipr.it

FIGURES AND TABLES

Table 1. Mechanical properties of AISI 4140 steel.

MATERIAL	σ_y [MPa]	σ_u [MPa]	ε_u [%]	$HV\left[\frac{kg_f}{mm^2}\right]$
AISI4140	689	900	178	320

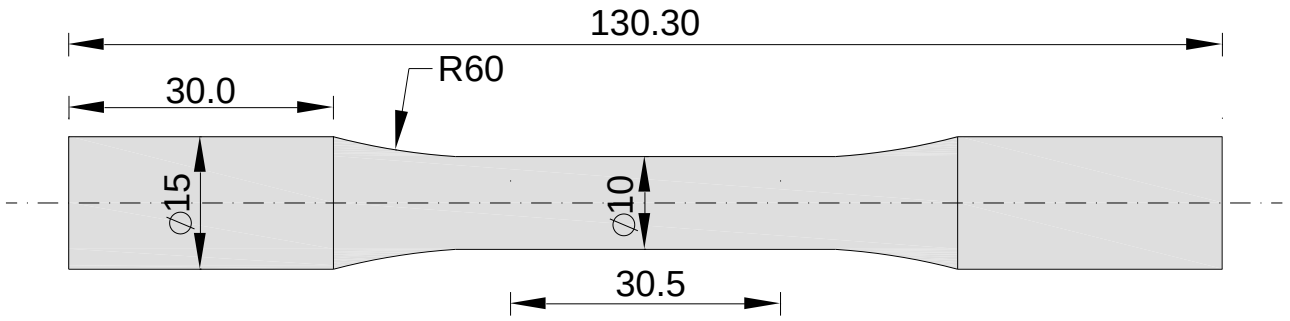

Figure 1. Geometry of the specimen according to the ASTM International E466-15 (sizes in mm).

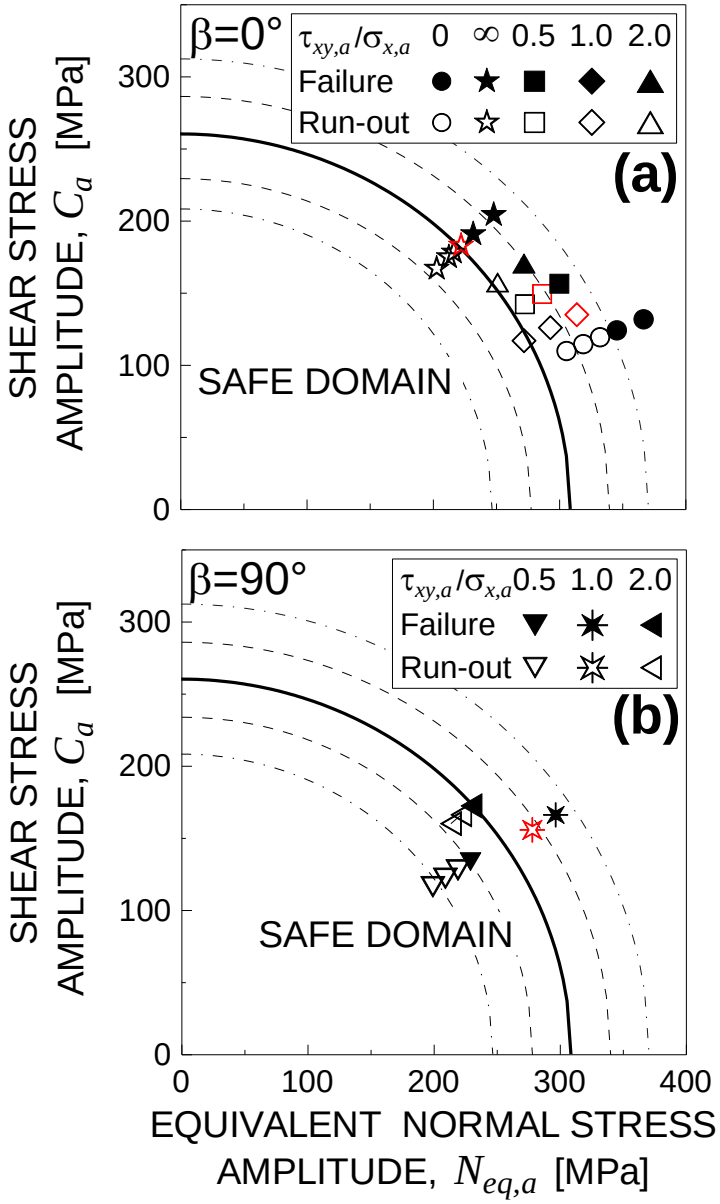

Figure 2. Shear stress amplitude vs. equivalent normal stress amplitude acting on the critical plane: theoretical predictions and experimental data. The volume associated to the useful cross-section is equal to $V_1 = 2400 mm^3$.

Table 2. Mean value of the error index, $\bar{I}$, by employing the Findley criterion [49], the MWCM [50] and the present methodology.

	Findley [49]		MWCM [50]		Present study	
Phase shift, β [°]	0	90	0	90	0	90
Error index, $\bar{I}$ [%]	15.3	18.4	12.0	22.7	8.2	-5.4

Table 3. Fatigue strength under normal and shear loading and mean value of the error index by varying the volume associated to the useful cross-section.

Volume, V	V value $[mm^3]$	σ_{wl} [MPa]	τ_{wl} [MPa]	$\bar{I}$ [%]
V_1	2400	309	260	1.4
V_2	24000	302	254	3.4
V_3	72000	298	251	4.5
$V_{crankshaft}$	7.9E+09	274	231	13.9
V_{opt}	954.19	313	263	0
Exp. tests	-	375	282	-11.8

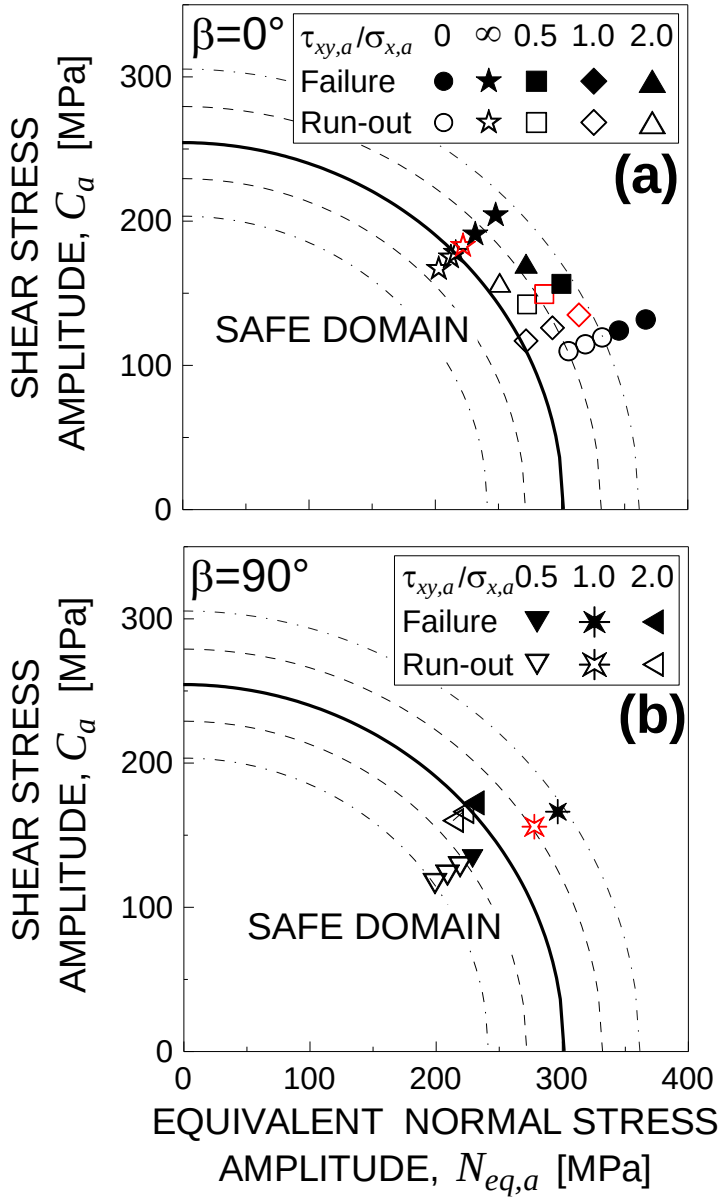

Figure 3. Shear stress amplitude vs. equivalent normal stress amplitude acting on the critical plane: theoretical predictions and experimental data. The volume associated to the useful cross-section is equal to $V_2 = (10) \cdot 2400 mm^3$.

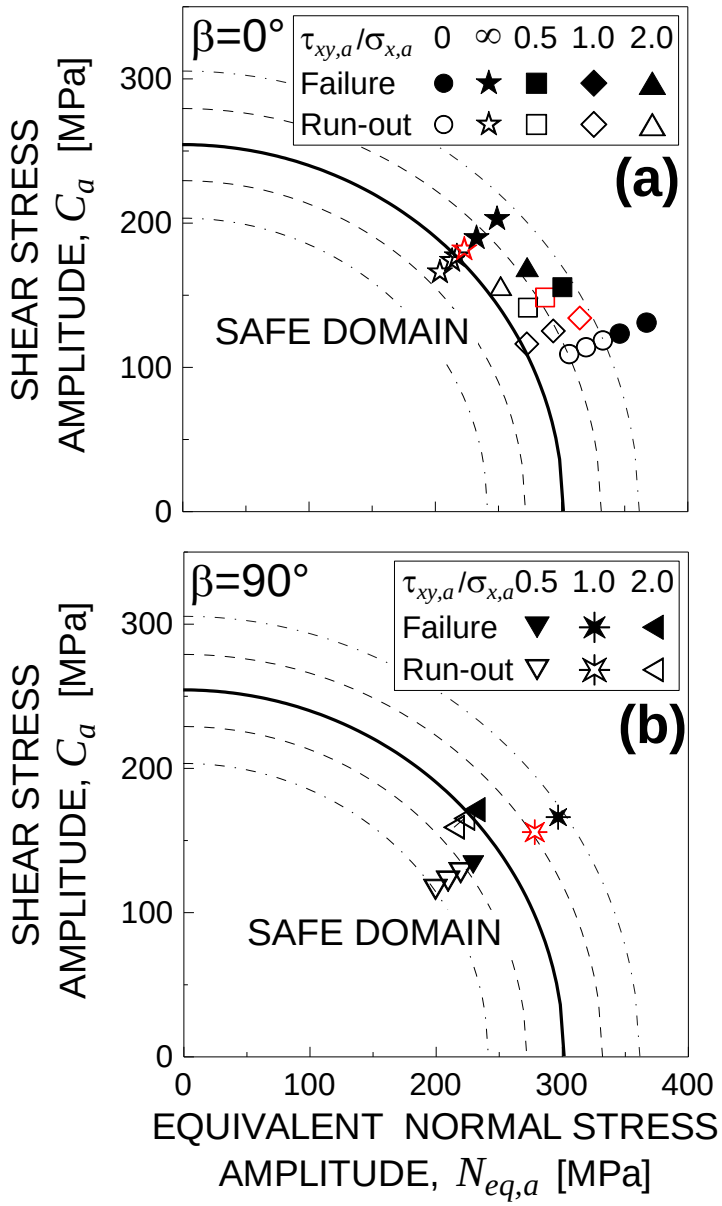

Figure 4. Shear stress amplitude vs. equivalent normal stress amplitude acting on the critical plane: theoretical predictions and experimental data. The volume associated to the useful cross-section is equal to $V_3 = (30) \cdot 2400 mm^3$.

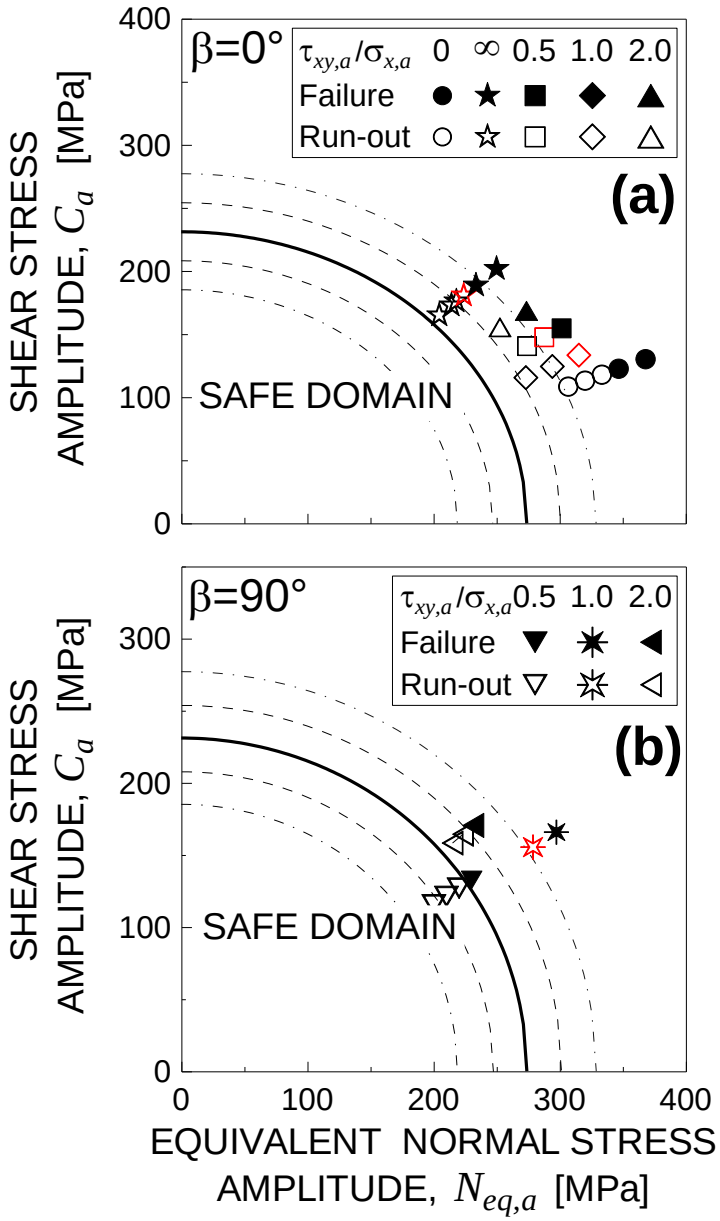

Figure 5. Shear stress amplitude vs. equivalent normal stress amplitude acting on the critical plane: theoretical predictions and experimental data. The volume associated to the useful cross-section is equal to that of the examined crankshaft, $V_{crankshaft}$.

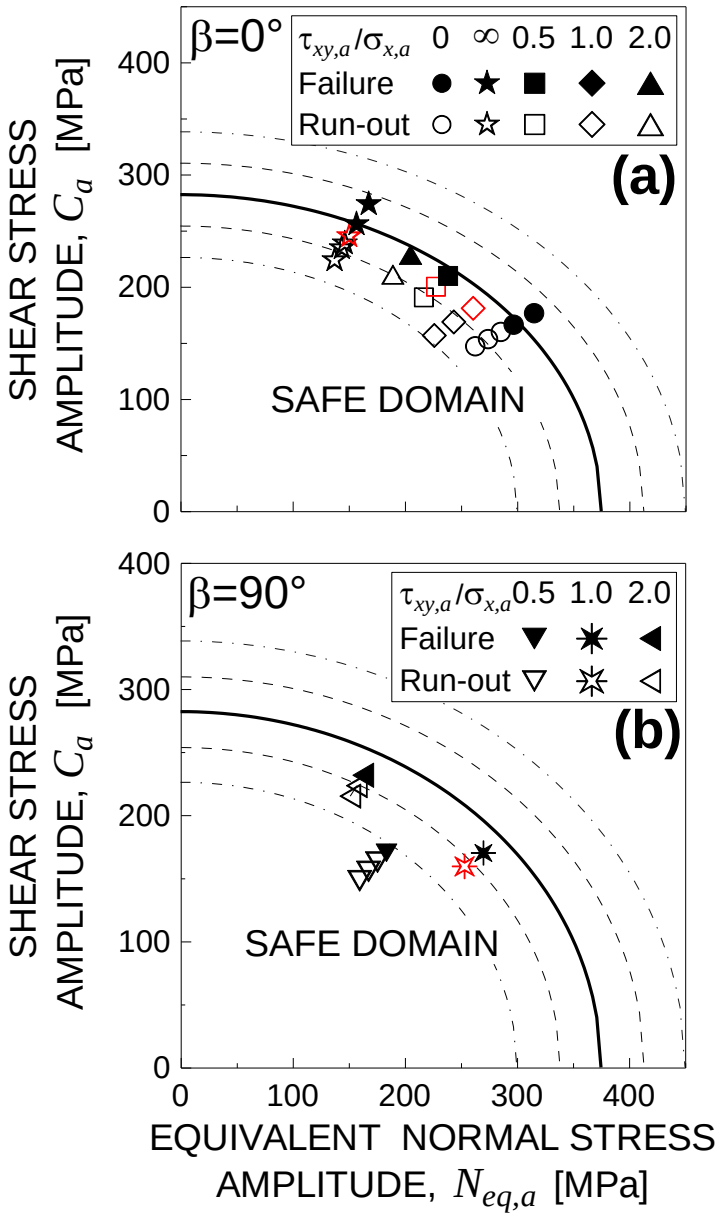

Figure 6. Shear stress amplitude vs. equivalent normal stress amplitude acting on the critical plane: theoretical predictions ($\sigma_{wl} = 375MPa$, $\tau_{wl} = 282MPa$) and experimental data.

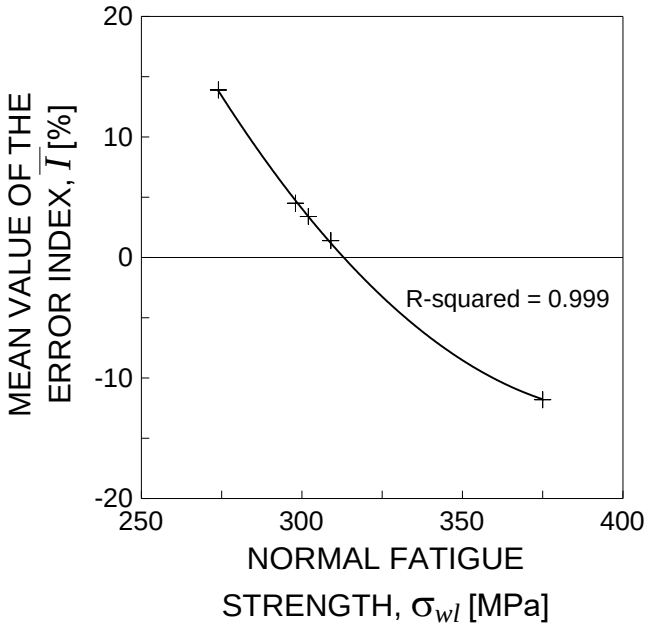

Figure 7. Mean value of the error index vs fatigue strength under normal loading for different values of the volume associated to the useful cross-section.

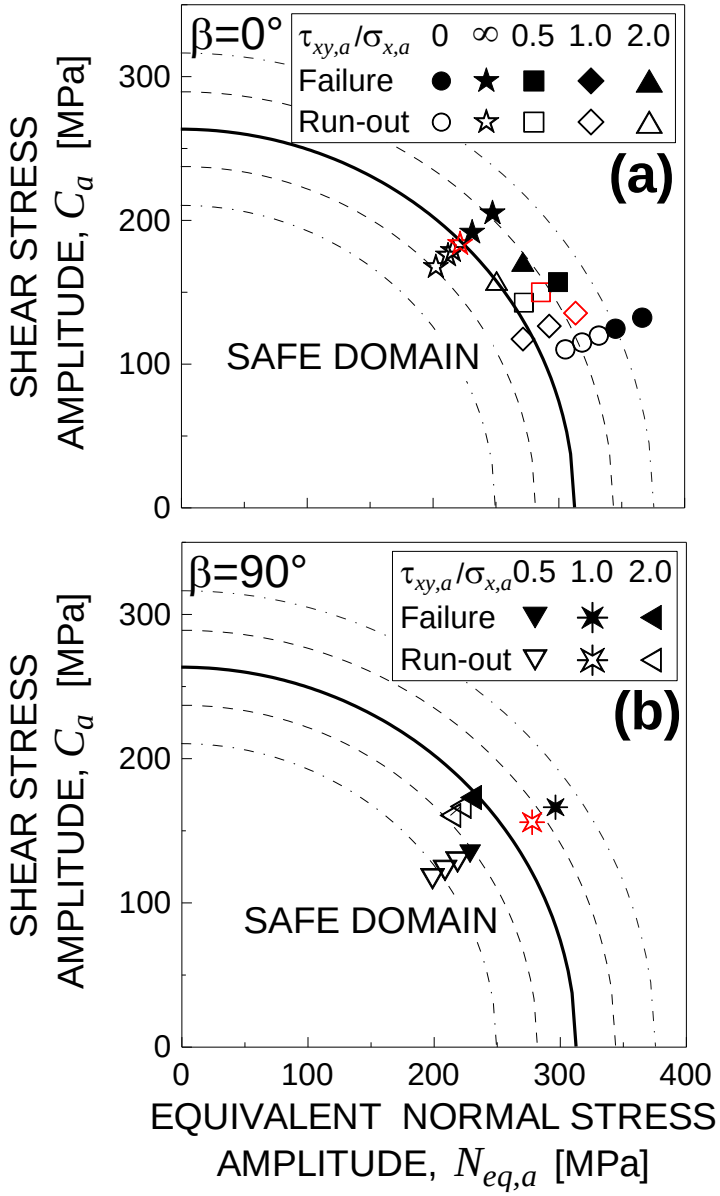

Figure 8. Shear stress amplitude vs. equivalent normal stress amplitude acting on the critical plane: theoretical predictions and experimental data. The volume associated to the useful cross-section is equal to the optimised volume, V_{opt}.